

Research Article

Derivation of Geodesic Flow Fields and Spectrum in Digital Topographic Basins

Sin Liang Lim¹ and B. S. Daya Sagar²

¹ Faculty of Engineering and Technology, Multimedia University, Melaka Campus,
Jalan Ayer Keroh Lama, Bukit Beruang, Melaka 75450, Malaysia

² Documentation Research and Training Centre (DRTC), Indian Statistical Institute-Bangalore Centre,
8th Mile, Mysore Road, RV College PO, Bangalore, Karnataka 560059, Bangalore, India

Correspondence should be addressed to Sin Liang Lim, lim.sin.liang@mmu.edu.my

Received 9 October 2007; Accepted 14 May 2008

Recommended by Marko Robnik

We present a framework to characterize terrestrial functions—surficial and bottom topographic regions that are represented, respectively, as raster digital elevation models (DEMs) and digital bathymetric models (DBMs)—through analysis of flow fields that are simulated via geodesic morphology. Characterization of such functions is done via a new descriptor. Computation of this new descriptor involves the following steps: (i) basin in digital form representing topographic fluctuations as an input, (ii) threshold decomposition of basin—that consists of channelized and nonchannelized regions—into sets, (iii) proper indexing of these sets to decide the marker set(s) and its (their) corresponding mask set(s), (iv) performing geodesic propagation that provides basic flow field structures, and (v) finally providing a new basin descriptor—geodesic spectrum. We demonstrated this five-step framework on five different synthetic and/or realistic DEMs and/or DBMs. This study provides potentially invaluable insights to further study the travel-time flood propagation within basins of both fluvial and tidal systems.

Copyright © 2008 S. L. Lim and B. S. D. Sagar. This is an open access article distributed under the Creative Commons Attribution License, which permits unrestricted use, distribution, and reproduction in any medium, provided the original work is properly cited.

1. Introduction

Remote sensing technologies offer highly promising tools that can be efficiently employed to generate digital topographies that include both surficial elevation and bathymetry. These technologies have flexibility in terms of repetitive coverage and can also be used at episodic intervals to map the possible topographic zones. With such provisions, it is now possible to study the morphodynamics of topographies. The two significant challenging steps involved in understanding the basin morphodynamical processes include: (i) mapping topographies of basins, bays, lakes, estuaries that are conspicuous at land-sea confluence using remote sensing

technologies, and (ii) characterization of those digital topographies in both multiscale and multitemporal modes. To address the latter step, a geodesic function of the basin, a new basin descriptor, has been proposed in this paper. Hereafter, “basin” interchangeably refers to inland, tidal, floodplain, coastal, and estuary regions, and digital topographies that include DEMs and DBMs, and “topography” refers to both surficial and bottom topographies. High-resolution DEMs and DBMs offer several advantages for modeling, simulation, and characterization of various surficial and bottom topographic morphodynamical processes. A brief review on the available approaches (i) to generate and/or map surficial and bottom topographies using several remote sensing techniques and (ii) to characterize such digital topographic basins is given as follows.

During recent past, a reasonably convincing success has been achieved in mapping the topography and bathymetry of fluvial and tidal environmental zones essentially above mean sea level, bays, estuaries, and certain shallow water regimes such as lakes, tidal inlets, and basins, by employing remotely sensed data acquired through different mechanisms (e.g., Lidar, satellite altimetry, SAR interferometry, etc.). During the last decade, several researchers addressed the topic of generation of topographic elevation maps and mapping of bathymetry zones using remotely sensed data. With advent of interferometry techniques, it is now possible to generate high-resolution DEMs precisely by taking the advantages of various remote sensing principles [1, 2]. In general, the techniques and/or mechanisms involved in acquiring the images suitable for mapping bathymetry include spaceborne and airborne data [3]. Aircraft-based Lidar bathymetry has the advantage of gathering data more quickly than an echosounder. IRS-1D LISS-III data have been used for bathymetric mapping purpose [4]. Geophysical Environmental Research (GER) Imaging Spectrometer was used to acquire hyperspectral data to map bathymetry remotely for the Hudson estuary waters [5]. Low-cost airborne multispectral remote sensing system is designed and evaluated for shallow water bathymetry purpose [6]. Eventually, bathymetric assessment system (BAS) is proposed for bathymetric mapping in shallow seas using radar images integrated with echosounding data [7]. It was reported that there exists a relationship between sea surface temperatures and bathymetry. SSTs are usually warmer in shallow areas [8]. Landsat Thematic Mapper (TM) data and ERS-1 SAR data have been systematically used to map lake bathymetry [9]. Preliminary results of along-track interferometry (ATI) observations over the Tay estuary validated with coincident in situ boat-based observations are presented [10]. Digital satellite altimetric bathymetric grid of the ocean was generated by combining high-resolution marine gravity information with depth soundings collected over the past 30 years [11]. Having mentioned this brief review on success of application of remote sensing technologies in mapping both surficial and bottom topographies, it is realized that to great extent the topographic mapping studies are established. Several applications were shown by employing DEMs and DBMs of multitemporal scales to address various problems of interest to remote sensing and geoscientific communities. From characterization point of view, several researchers proposed methods to partition the digital topographies into basins of varied orders [12, 13]. These basin-wise digital topographies that include both surficial and bathymetry zones are characterized via various techniques [14–18]. Important basin descriptors that can be derived from DEMs include morphometry, hypsometry, cumulative area distribution, and width function-based descriptors [19]. Other widely studied mathematical properties—in the context of understanding the random functions of geophysical relevance (e.g., digital topographies such as DEMs and DBMs) include geomorphic width function, convexity measures

of travel-time networks, granulometric indices, morphometry of nonnetwork spaces [20–24].

Spatial resolution of DEMs and DBMs is an important aspect particularly to deal with the processes involved in rather less-undulated terrestrial environments. Physical principles and mechanisms that are involved in controlling the dynamics (e.g., flooding and morphological variations) in fluvial and tidal systems are different from each other. The two examples of less-undulated regions of significance include floodplain and tidal environments, in which the regions are rather flat. If high-resolution DEMs and DBMs for these regions are available, several physical processes involved in floodplain and tidal environments could be modeled in an efficient manner. In basins, the flooding patterns follow simple propagation that could be solved with image-based geodesic morphologic equations. Due to tide level changes, in addition to flooding of time dependent tidal basins, understanding the time dependent sediment dispersal on the flat surface is an interesting phenomenon, which requires characterization of flow fields in discrete space. Simulations of basic flow fields within basin have generated interest in recent past. By employing classical shallow water equations, basic flow fields are simulated in small tidal basins [25]. In this work, entire basin is assumed flat, and the flow fields within which are simulated with simplified shallow water equations. In another study, sediment transport processes with flat and wavy bottom topographies are evaluated under the flow fields induced by the propagation of a tidal wave by employing partial differential equations [26, 27]. Generation of flow fields in shallow water regimes (e.g., floodplains and tidal environments) and coastal environments (e.g., bays, estuaries, lagoons) is an important study, which further facilitates to quantify the morphologic organization of topographic zones. Shallow water regimes such as lakes, ponds, coastal, and floodplain regions are considered to have rather flat topography. Conversely, the topography of fluvial basins, and bottom topography of several bays and estuaries (e.g., San Francisco Bay, San Diego Bay, etc.) are significantly heterogeneous. Perhaps, the flow fields simulated for shallow water regions, using simplified shallow water (hydrodynamic) equations [25], are valid.

The objectives of this study are as follows:

- (i) to provide a new geodesic spectrum-based basin descriptor by simulating flow fields via alternative approach with an assumption that topography is wavy,
- (ii) to characterize topography-dependent flow fields within a basin through geodesic flow spectrum, and
- (iii) to utilize the geodesic flow fields to derive probabilities and entropy values to characterize the topographic regions of varied types.

Towards achieving these objectives, this paper is organized as follows. Section 2 discusses the general assumptions in the model and representation of basin as discrete function, and its decomposition into sets as well as certain basic mathematical (geodesic) morphological transformations. Section 3 explains the model assumptions and the approach followed to index sets to simulate geodesic flow fields in basins. In Section 4, geodesic flow fields—simulated by considering the successive threshold elevation regions (TERs, sets decomposed from discrete functions) as marker and mask sets—are employed to derive probabilities and entropy values to characterize the topographic regions of varied types. Results and discussion, and concluding remarks are given, respectively, in Sections 5 and 6.

2. Methodology

To accomplish the objectives, elevation-dependent flow fields are simulated via geodesic morphologic transformations. Further, the probabilities of areas embedded between the successive flow fields are estimated to quantitatively characterize the flow fields with TERs with respect to their corresponding basin.

2.1. Model and motivation

The principle involved in simulating geodesic flow fields is flood propagation within a basin. Geodesic propagation mimics the flood propagation within a basin. Floodwaters or the water flow into higher elevation regions from the tidal inlets propagates from region with lowest elevation to successive higher-elevation regions. Such propagation can be simulated by following geodesic morphologic transformations and by considering the digital topographic data (e.g., DEMs and DBMs) that can be derived as by-products of remotely sensed satellite data sources. These flow fields facilitate a way to characterize basin topographies. These flow field simulations are valid under the assumption that the river flow is weak in such a way that extreme flood flow forcing dominates the weak river flow. For example, this assumption is valid under the influence of neap/spring tidal cycles. The extreme tidal forcing conditions are twofold: (i) when tidal forcing dominates the weak river flow, and (ii) when river flow dominates the low tidal forcing. Under the circumstances that tidal or flood forcing dominates the river flows, the tidal or flood water flows through the inland basin.

From basin point of view, the propagation velocity of waterfront would vary with the TERs. Basin with flat surface includes both channelized and nonchannelized regions with similar elevations with reference to Mean sea level. Simulations of flow fields in such a flat basin (e.g., see Figure 1(a)) can be achieved with ease by employing rather straightforward and simplified shallow water equations [25]. In realistic case, channelized regions are the first level topographic depressions that are relatively with lesser elevations than that of their corresponding nonchannelized regions (see Figures 1(b) and 1(c)). It is intuitively true that the channel network within the basin supports that the waterfront propagates at rapid state relatively with that of nonchannelized regions, due to the fact that the nonchannelized region is relatively with higher gradient. To support this valid argument, classification of the basin into zones according to certain characteristics is required. These characteristics include the changes in slope, bathymetry, soil characteristics, and roughness of the topography. Intuitively, it is also true that the propagation would be uniform in nonviscous flat surface. Within the environment with different viscous characteristics, modeling the waterfront propagation essentially requires geodesic balls with different radii synchronising the changes in surficial characteristics.

2.2. Data

The three synthetic cases (see Figures 1(a)–1(c)) with varied internal topographic regions that replicate the (i) flat, (ii) undulated without channels, and (iii) with channels conspicuous in topography are considered. In reality, these three cases mimic, with the following assumptions, topography of shallow water regimes (e.g., shallow lakes with flat bottom topography), bays and estuaries, and basins of floodplains and tidal environments.

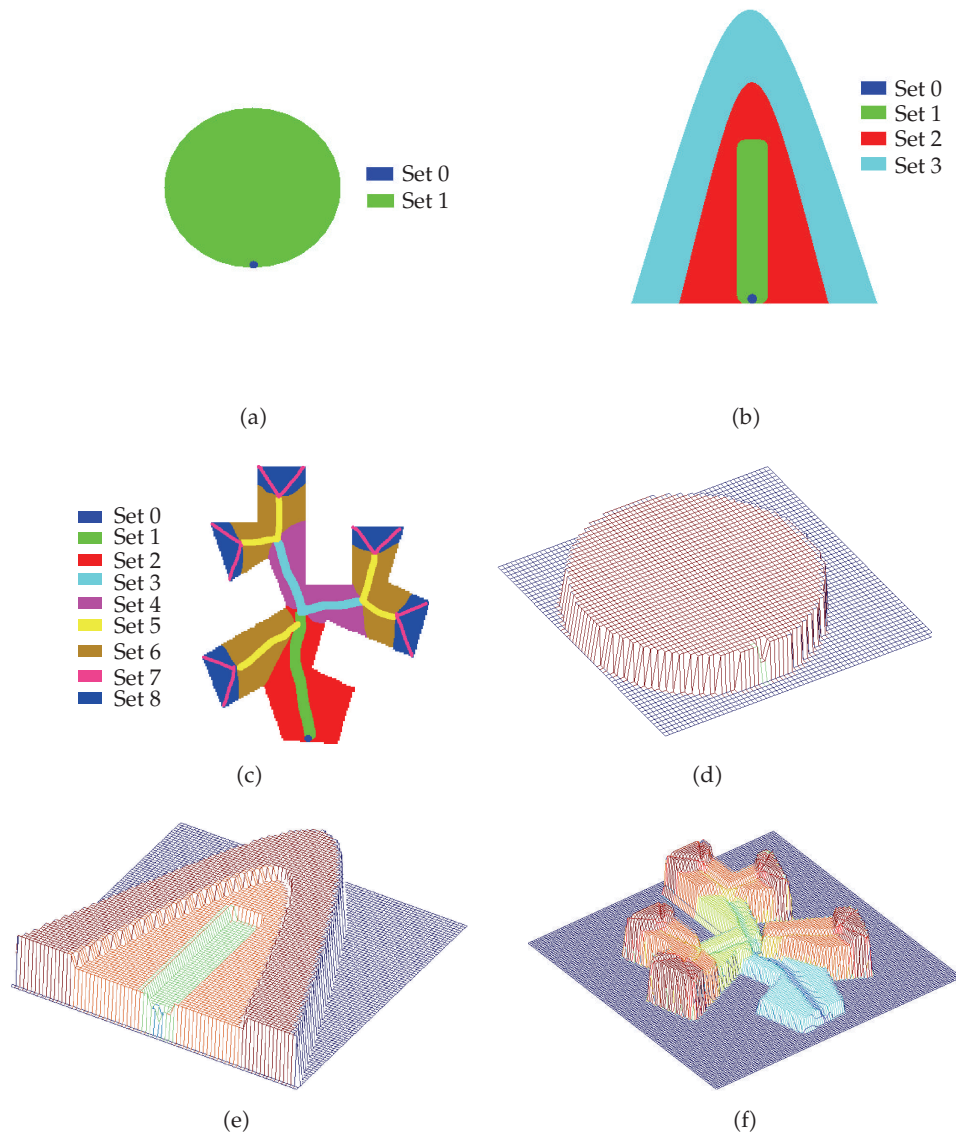


Figure 1: Tidal basins with different assumptions: (a) flat tidal basin, (b) tidal basin with a channelized and nonchannelized zones (multiple sets of topological significance), and (c) tidal basin with multiple sets, sets indexed with even and odd indexes, respectively, refer to channelized and nonchannelized zones. (d)–(f) 3D mesh representations of three synthetic tidal basins shown in (a)–(c).

Case 1. Single inlet, from which the water propagates uniformly within the mask set (see Figure 1(a)). With this assumption, oscillations in tidal levels and forcing influence the whole tidal basin that is assumed to be flat. Typical unidirectional flow propagation patterns are shown in Figure 6(a).

Case 2. Single inlet, from which the water would first flow into channelized regions of uniform elevation followed by inland region. Here, channelized set and inlets (see Figure 1(b)) are with different elevations. Nevertheless, in contrast to Case 1, flow fields in channelized sets maintain orthogonality with the flow fields in nonchannelized sets. This is both physically and

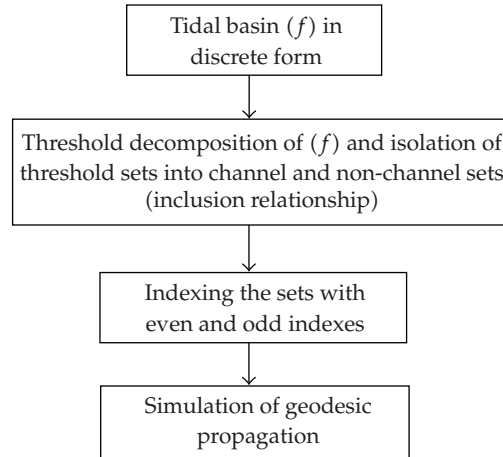


Figure 2: Flowchart depicting various steps involved in modeling and simulation.

intuitively justified due to the fact that flow propagation in channelized zones precedes flow propagation in nonchannelized regions.

Case 3. Single inlet and water flows alternatively into channel region and into inland until the propagating waterfronts reach the basin boundary (see Figure 1(c)). Criteria followed to simulate flow fields—satisfying the fact that channelized and nonchannelized regions are relatively with different mean elevations—include the following. Let M be the set of one channel, and it makes an arborescence from the inlet point from which the water flows into channels and their inlands which is therefore the base of the trunk of the tree. This tree is connected, by definition, because we work on one channel set, where the water flow is coming up uniquely. Each branch is assimilated to a segment (if not, we subdivide the branch into a short succession of segments based on the following criteria (i) the mean elevation, (ii) width of segments, (iii) direction of flow, and (iv) the depths by taking the structure of an ascending tree). Then disconnect each branch, by removing its first point (that of the subdivision with the upstream branch). Then compute the skeleton by zones of influence of the disconnected branches to obtain the non-channelized zone associated with each branch (i.e., with each channel). It is similar to Figure 3. Figure 2 depicts various steps involved in the simulations.

Besides these synthetic cases, DBM of parts of Central San Francisco Bay and DEM of coastal Santa Cruz regions are considered.

(i) *Central San Francisco Bay bathymetry* data, acquired with multibeam system, have been utilized here with permission from USGS. The coastal San Francisco Bay's bathymetry—of 4 meter resolution and tide-corrected to mean low water level—has been acquired through multibeam sonar system that provides echo sounders with 60 beams, collected in 1997 using a Simrad EM 1000 multibeam swath mapping system [28, 29]. The region of interest in San Francisco Bay area, of size 512×480 pixels, encompasses approximately from $37^\circ 48' 41''\text{N}$ to $37^\circ 51' 34''\text{N}$, and from $122^\circ 26' 2''\text{W}$ to $122^\circ 29' 28''\text{W}$.

(ii) *Santa Cruz Digital Elevation Model.* The 10 meters grid spacing digital elevation map (DEM) of Santa Cruz, downloaded from San Francisco Bay Area Regional Database (BARD) homepage [30], provided by USGS is used. At a scale of 1:24000, it is available as 7.5 minutes standard DEM format on Universal Transverse Mercator (UTM) projection on North

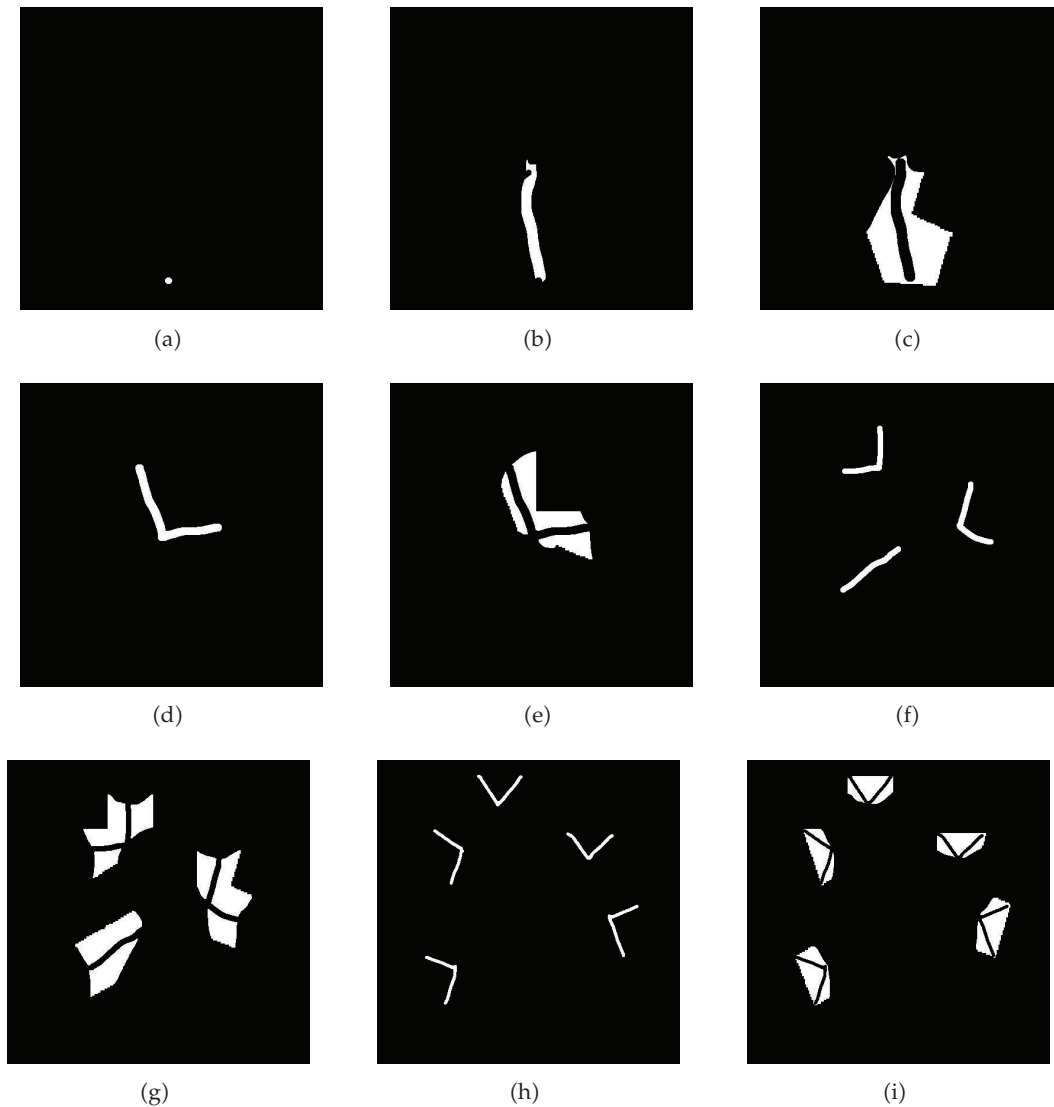


Figure 3: Synthetic tidal basin shown in Figure 1(c)—that consists of channelized and nonchannelized regions—after decomposing into sets. (a)–(i) sets representing channelized and nonchannelized regions of which the mean elevations increase from S_1 to S_9 . The sets with even- and odd-numbered indexes, respectively, represent the zones occupied by channelized and nonchannelized regions.

American Datum of 1927 (NAD 27), in the unit of meters for elevation relative to the National Geodetic Vertical Datum of 1929 (NGVD 29) [31]. The region of interest in Santa Cruz, of size 346×654 pixels, covers approximately from $36^\circ 56' 35''\text{N}$ to $37^\circ 00' 00''\text{N}$, and from $122^\circ 03' 56''\text{W}$ to $122^\circ 05' 38''\text{W}$.

2.3. Techniques

2.3.1. Decomposition of basins/threshold elevation and/or depth zones

Basin is denoted as a function (e.g., see Figures 1(a)–1(c)) represented by a nonnegative 2D sequence $f(m, n)$, which assumed $J + 1$ possible intensity values: $j = 0, 1, 2, \dots, J$. For 8 bit/pixel

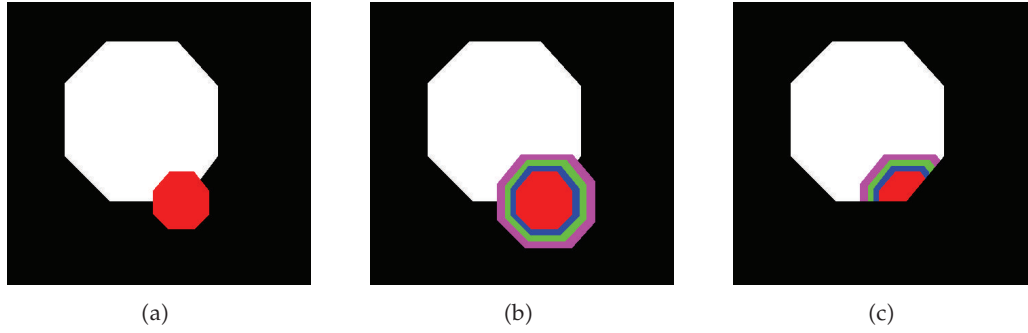


Figure 4: (a) Marker set S_i (in red) and mask set S_{i+1} (in white), (b) after iterative dilations up to fourth level superposed on the mask set S_{i+1} , and (c) the dilated marker set for four iterations intersected with mask set S_{i+1} .

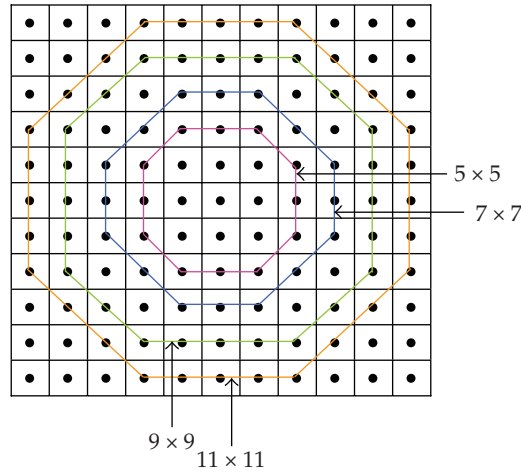


Figure 5: Octagonal symmetric structuring elements of various primitive-sizes ranging from 5×5 to 11×11 . These primitive sizes can be considered as B in the employed equations to simulate flow fields with various velocities.

digital topographic data, $J = 255$. The function, f (basin) is discrete, defined on a (rectangular) subset of the discrete plane Z^2 . The higher the intensity value is, the higher the topographic elevation is, and vice versa. This digital topographic data consist of various bounded sets that include inlet point, channelized and nonchannelized zones. By thresholding f at all possible intensity levels, in other words topographic elevations $0 \leq j \leq J$, we obtain threshold decomposed binary images or sets

$$f_j(m, n) = \begin{cases} 1, & f(m, n) \geq j, \\ 0, & f(m, n) < j. \end{cases} \quad (2.1)$$

Threshold sets, decomposed from basin, include both channelized and nonchannelized regions that take values 0 and 1 (the pixels with 1 and 0 represented with white and black shades denote, respectively, sets and their compliments). The sets (f_j) form a sequence of sets that characterize f entirely, and are such that for any threshold elevations j and $j + 1$ with $(j + 1) \geq (j) \Rightarrow (f_{j+1}) \subseteq (f_j)$, for j ranging between 1 and J —as illustrated in Figure 10. From

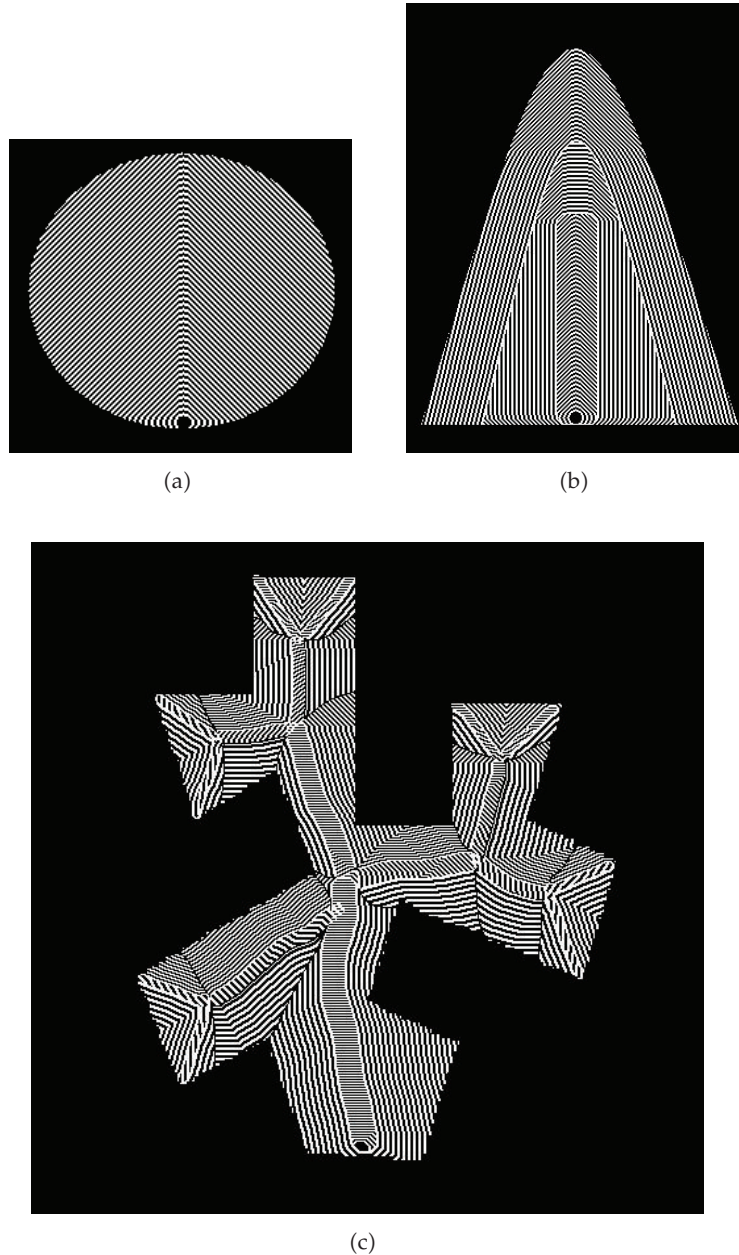


Figure 6: (a) Flow fields with isotropic propagation, (b) isotropic flow fields, and orthogonality between the flow fields of channelized and nonchannelized zones is obvious, and (c) flow fields within the tidal basin.

the point of basin's physiography, the elevations of inlet point(s) are lesser than that of the average elevation of successively decomposed channels, and basin's inland. By employing simple logical difference between the successive threshold-decomposed sets, we further obtain marker set(s) and its (their) mask set(s) according to $[f_j - f_{j+1} = S_i]$. Each threshold isolated set denoted by S_i is obtained via $f_j - f_{j+1}$, where $j = 1, 2, \dots, J$ and $i = 1, 2, \dots, J$. We decompose synthetic basin that consists of nine zones (see Figure 1(c)) into nine sets (see Figure 3) by specifying threshold elevations (values). These nine decomposed sets are designated with

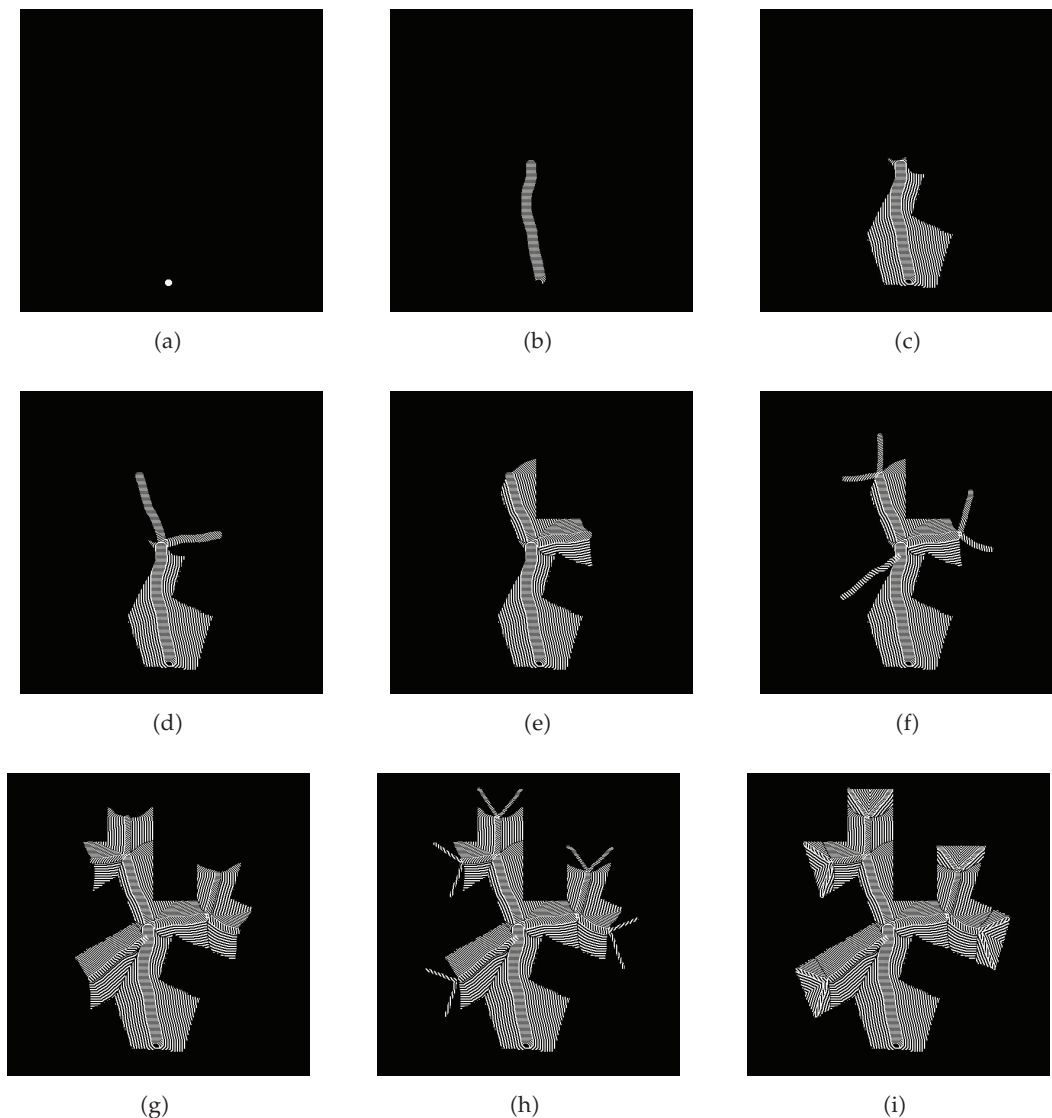


Figure 7: Result of simulation at different time instances. (a) inlet point or set S_1 from which the water flows into tidal basin, (b) water propagation from S_1 (marker set) into mask set (S_2), (c) flow fields propagating from marker-set S_2 into set S_3 —nonchannelized set or the influence zone of set S_2 —that acts as a mask set, (d) set S_4 the mask set that gets flooded due to the water flowing from the marker set S_1 after sets S_2 and S_3 are completely flooded, (e) set S_5 —nonchannelized (influence) zone of set S_4 gets flooded from the marker set S_4 , (f) set S_6 that acts as mask set to allow the water flows from the extreme tips of set S_4 , (g) set S_7 the influence zone of the channelized set S_6 —here the mask set S_7 would be progressively flooded from the water flowing from the marker set S_6 , (h) channelized mask set S_8 in which the water flows from the extremities of set S_6 , and (i) mask set S_9 —influence zone of set S_8 —gets progressively flooded due to water flowing from set S_8 that acts as a marker set to fill the water in its corresponding mask set S_9 .

set-orders ranging from 1 to 9 (see Figure 3). The union of these sets (f_j) and (S_i) satisfies the inclusion relationship [32] as shown in

$$f = \sum_{j=1}^J f_j, \quad f = \sum_{i=1}^J S_i. \quad (2.2)$$

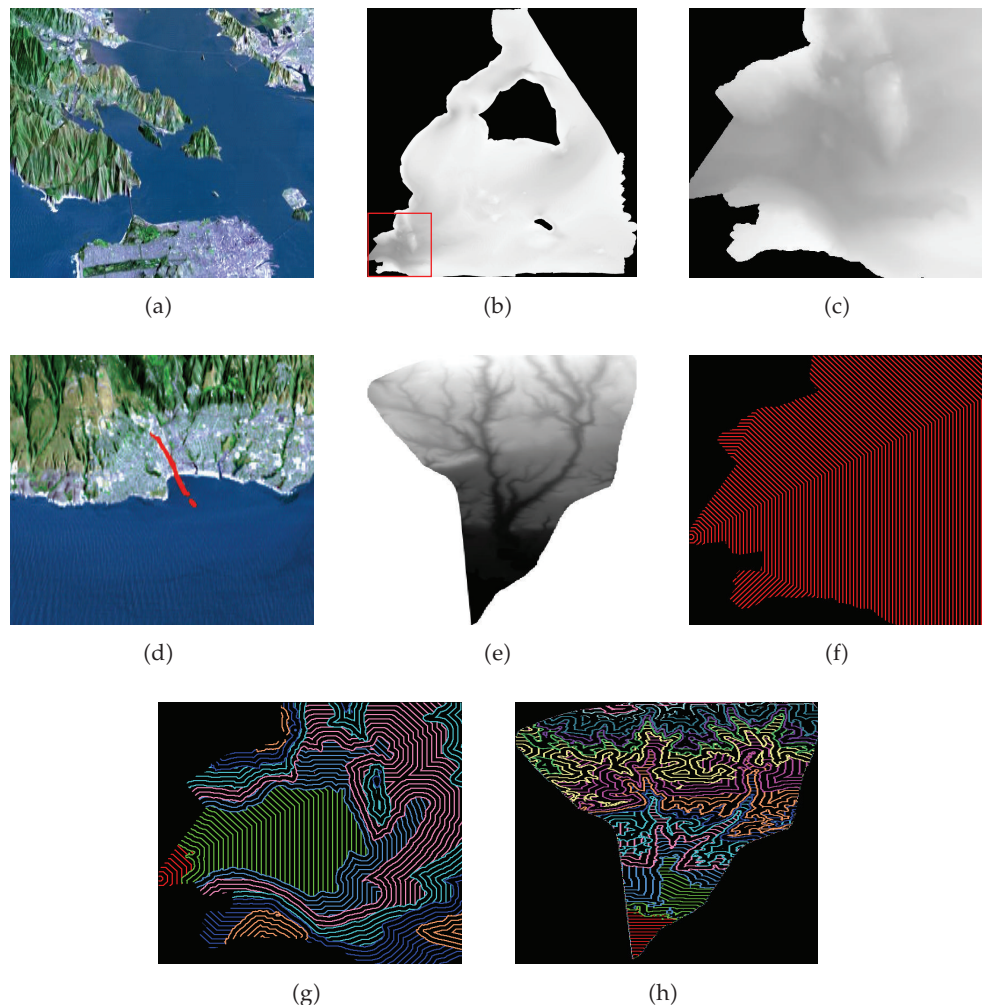


Figure 8: (a) 3D view of remote sensing data of Central San Francisco Bay, (b) bathymetry of Central San Francisco Bay, (c) bathymetry of inset of (b), (d) 3D view of Santa Cruz, and (e) Digital elevation map of Santa Cruz, (f) flow field simulated on San Francisco Bay without considering bathymetry, (g) flow field simulated on San Francisco Bay bathymetry by using octagon, and (h) flow field simulated on Santa Cruz DEM by using octagon structuring element.

For simplified representation, we denote the subtracted sets thus obtained, respectively, with $S_i, S_{i+1}, S_{i+2}, \dots, S_J$, with i ranging from 1 to J (see Figure 3). Set S_1 denotes the inlet point. The set with immediate higher index acts as mask set to the marker set with preceding index. For better understanding of threshold decomposition and isolation of sets, reader may refer to Figure 10.

2.3.2. Geodesic propagation methods

We adopt geodesic morphological transformations [33]. James Sethian's [34] level set theory and Jean Serra's [35] random sets and mathematical morphologic concepts offer various transformations to simulate flow fields within basin with physical viability. To implement geodesic transformations, we consider basin as a mask, and inlet point—through which water flows

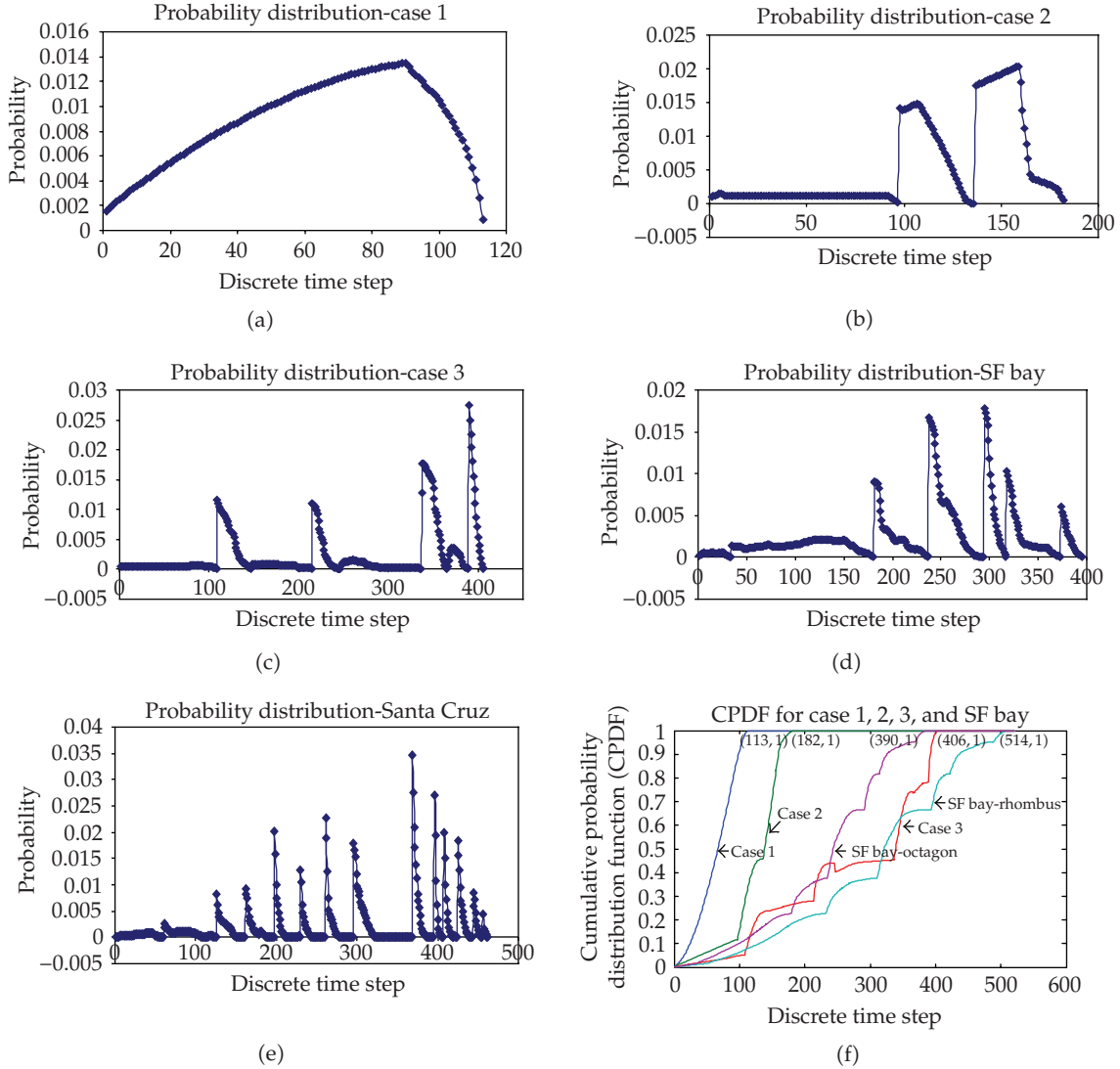


Figure 9: Probability of estimated area flooded at each discrete time step. The flow propagation for the 3 cases is simulated by using rhombus as structuring element, while flow fields for San Francisco Bay and Santa Cruz are simulated with the use of octagon as structuring element. (a) case 1, (b) case 2, (c) case 3, (d), San Francisco Bay, (e) Santa Cruz, and (f) cumulative probability for total area flooded.

into basin during the high flood—as a marker from which the flow propagates into the basin as the flood-level increases. To implement geodesic propagation with uniform velocity within a mask (set S_{i+1}) with certain boundary conditions from the marker set (set S_i), we employ (i) morphological dilation iteratively on S_i with a structuring element (B) of symmetric about the origin, and of primitive size 5×5 , (ii) logical intersection between the dilated marker S_i and mask S_{i+1} sets, and (iii) logical union of flow fields at respective discrete times.

2.3.2.1. The morphological dilation of S by B is defined as a transformation that combines S and B using vector addition of set elements s and b , respectively, with $s = (s_1, \dots, s_N)$ and $b = (b_1, \dots, b_N)$ being N -tuples of element coordinates. Then, the dilation of S by B is the set of all possible vector sums of pairs of elements, one coming from S and the other from B . The

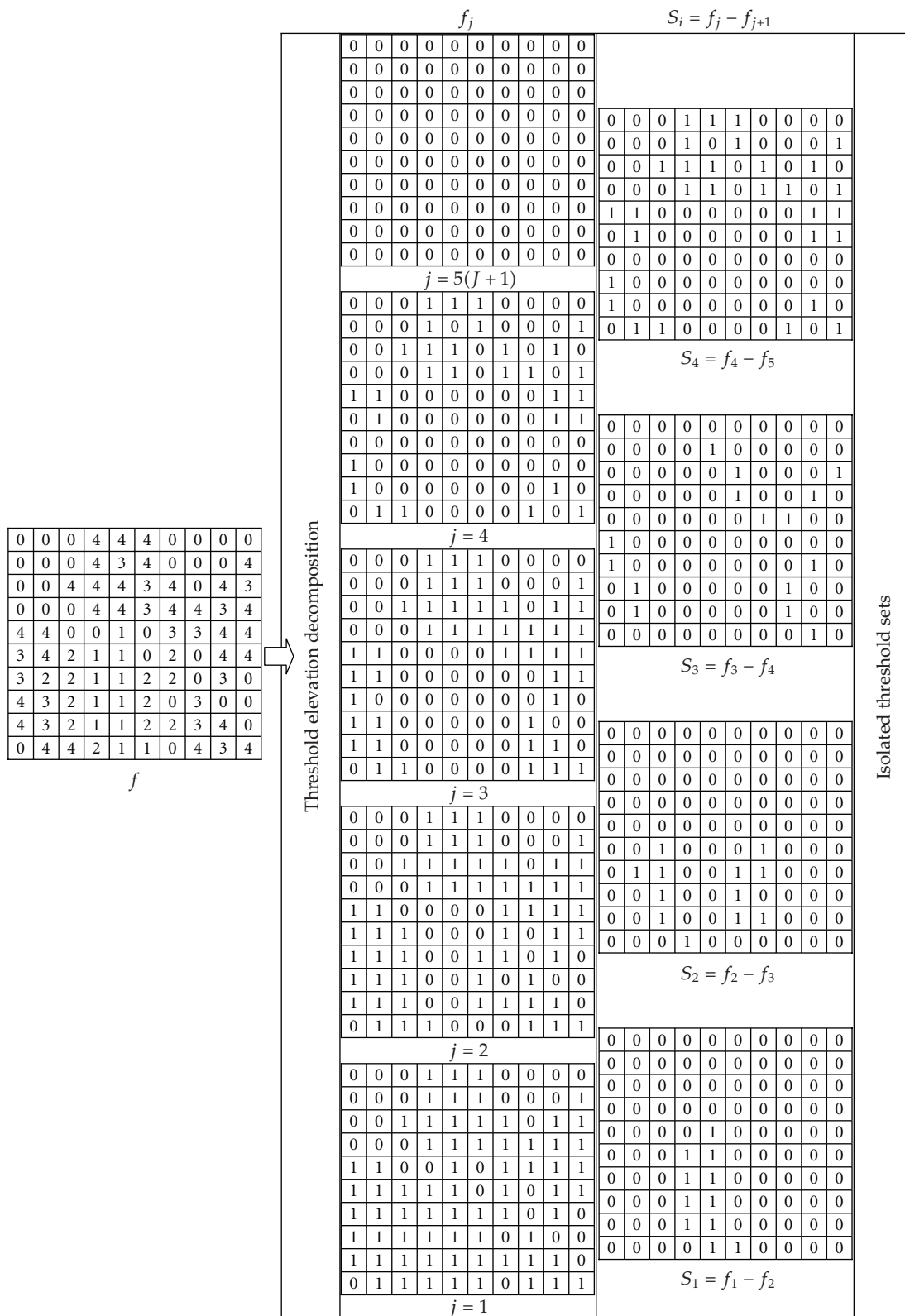


Figure 10: Original image f has maximum intensity level $j = 4$. Threshold decomposed zones f_j with $j = 1, 2, 3, 4$, and 5 ($J + 1$) are, respectively, shown along with the isolated sets with index i ranging from $1, 2, \dots, j$. The sets S_i are isolated by $f_j - f_{j+1}$.

primitive structuring element) and set $(S_{i+1}$ —with which the propagation pattern should intersect) size dependent. The marker set should be included in the mask set. If the intersection of mask set with which the flow field that should propagate from the marker set to mask set produces an empty set, we should not consider such a mask set. Then, we have to proceed further to consider mask set that is decomposed with the next higher threshold value. We take S_i and S_{i+1} as marker and mask sets if $(S_i \oplus nB) \cap (S_{i+1}) \neq \emptyset$. If $(S_i \oplus nB) \cap (S_{i+1}) = \emptyset$, we do not choose S_i and S_{i+1} , respectively, as marker and mask sets. Instead, we check $(S_i \oplus nB) \cap (S_{i+2})$ whether the intersection is nonempty set to consider S_i and S_{i+2} , respectively, as marker and mask sets. If there are two marker sets with similar threshold value, we need to ignore one of the marker sets that is fully surrounded by the mask set.

In a flat basin, where there is no distinction between channelized and nonchannelized regions in terms of elevations (e.g., see Figures 1(a), 1(d)), the total flow field can be defined in morphological terms as the intersections of gradients of successively dilated marker set with the mask set. n th-time step gradient, $\delta^n(S)$, between the successively dilated marker set is defined in

$$\partial^n(S) = \left[(S_i \oplus (n+1)B) \setminus (S_i \oplus nB) \right], \quad (2.6)$$

where, nB , $(n+1)B$, respectively, denote forcing in terms of structuring element with different sizes. The primitive structuring template of size 5×5 is considered as a unit to simulate flood forcing. The flood flows into channel from the inlet point as time progresses. This progression in the flow is simulated by B , by iterative dilations, and by means of B until idempotence; in other words, until the intersection of gradient with mask set becomes an empty set. Alternatively, one can write in terms of $\partial^n(S_i)$, this positive integer $N = \max\{n : [\partial^n(S_i) \cap S_{i+1}] \neq \emptyset\}$ such that $\{[\partial^{n+1}(S_i) \cap S_{i+1}] = \emptyset\}$, for the flow for all $n > N$. This N depends on S_i , S_{i+1} , and B . The flow field at n th discrete time step is defined as the line that is obtained by intersecting the n th time-step gradient $\partial^n(S_i)$ with the mask set (S_{i+1}) . The propagation of flow field after n th time-step is simulated by intersecting the gradient—computed according to (2.5)—with the mask set (S_{i+1}) . The progression in time, denoted with increments of $n = 0, 1, 2, \dots, N$, is related to the size of B . The larger the cumulative effect of flood forcing at successive discrete time steps, the larger the size of the B . Then, the total flow field in the simplest Case 1 (see Figures 1(a), 1(d)) can be achieved by (2.7). In order to visualize the flow fields within the channelized and nonchannelized zones (or sets), a logical union operation is considered in the respective governing equations:

$$TB_{\text{flow}} = \bigcup_{\substack{n \geq 0 \\ i \geq 1}}^J \{[\delta^n(S_i)] \cap S_{i+1}\}, \quad (2.7)$$

where $i = 1, 2, \dots, j$, $n =$ discrete time (with time effect of cumulative flood forcing increases), and also n denotes the size of the structuring element and the discrete time, and the limit of N is the iteration step at which the idempotence is reached. The increment in n defines the increase in size of structuring element, in other words the cumulative flood forcing. The gradients between the successively dilated sets are intersected with mask set S_{i+1} . Once this process reaches idempotence, the flow propagation simulation proceeds further in the succeeding mask set S_{i+2} .

3. Simulations of geodesic flow fields

To study the morphodynamic problems in the coastal and tidal environments—where the flow fields' structure is greatly influenced by fluctuating tidal/flood forcing and river water inflows—it is necessary to describe the spatiotemporal structure of the flow fields. The flow field simulations are done here, with an input of digital topographic regions available in raster format, by using proposed geodesic dilation-based algorithm. The term “flow field” refers to any water frontline propagating towards immediate spatially distributed elevation regions. The flow fields propagate from inlet point (initial marker) into channels along the medial axis direction with greater velocity along the medial axis line than along the channel walls. In order to justify this hydrodynamically viable assumption, we adopt a structuring element of octagon in shape, symmetric about origin and of primitive size 5×5 (see Figure 5) to simulate flow field propagation. However, the velocity variations can be imposed by tuning characteristics of structuring element while changing the (i) medium from channelized set to nonchannelized set, (ii) tidal forcing, (iii) elevation, (iv) spatial positions of source(s) of inlet(s), and (v) direction of flow. Tide with exceeding velocity (forcing) inundates the tidal basin's inland. For instance, due to these factors, the geodesic ball that would be used to model propagation within the channelized region would be relatively with larger radius compared to that of required radius of geodesic ball to model the water propagation in the nonchannelized regions. A directional propagation is obtained when ball B is a unit segment in the direction of propagation. If we use a digital disc for B (e.g., see Figure 5), the propagation is necessarily uniform. One can alternate unit segment and unit disc if a mixture is required, but at the idempotent limit the result will be that of the disc propagation.

Case 1. In a basin, with assumptions that channels and inlands are of same elevation, flow fields propagating in unidirection can be simulated by following geodesic-based equations (2.5) and (2.6). The flow of propagating water synchronizing the tidal/flood forcing is like a sheet of water flowing on a flat surface from the inlet source. The gradients of such propagating fronts (dilated versions) at discrete intervals are shown in Figure 6(a), where the circular path and inlet set act respectively like the boundary conditions and flow propagation source. Flow field complexity depends not only on basin shape and general topography/bathymetry, but also on the spatial organization of channels within basin. Flows in channels and nonchannelized regions of basins are simulated by following geodesic propagation methods. The latter two cases are modeled based on the assumptions that the channels are the first level zones that get affected by fluctuating tides/flood intensity and followed by nonchannelized regions that are relatively with less depth. Flow field propagation would be in the channelized regions of lower threshold decomposed region (S_i) first followed by in the nonchannelized region of S_{i+1} , eventually, in the channelized region of say S_1 , and then in the nonchannelized region of S_2 , and so on. The flow propagation pattern in basin is categorized as (i) propagation in channelized region, and (ii) propagation in nonchannelized zones.

Case 2. In this case, the propagation of flow fields in channelized sets is orthogonal to that of corresponding nonchannelized sets. The geometric and spatial organizations of flow fields within channelized regions are different from that of their corresponding nonchannelized regions. Hence, the equations governing the flow fields are indexed-set dependent. For the second case of flow field simulations, we consider (2.5)–(2.7), in which marker and mask sets

are recursively changed in the fashion of i th and $i + 1$ th sets, act respectively as marker and mask sets.

Case 3. However, the flow fields in the basin's inland propagate in the direction perpendicular to that of channels. The channels, the first level zones that are affected by fluctuating stream flow discharges and/or tides, and nonchannelized regions surrounding the channels are relatively with different depths/heights. Flow fields' directions and spatial complexity depend not only on basin shape and general elevation structure, but also on the spatial organizations of channels and inlands. For the third case of flow field simulations, we consider set with index $i = 1$ as a marker and is allowed to geodesically propagate (e.g., see Figure 4) within the mask set indexed with $2i$. For simplified representation, we denoted the threshold decomposed sets thus obtained (see Figure 3) as $S_i = S_1, S_2, S_3, \dots, S_J$ with i ranging from 1 to J . This notation is done to explicitly write the equations in such a way that the channels and their corresponding inlands can be respectively represented with even and odd i th values. In the third case (see Figures 1(c), 1(f), 3), certain sets are order designated as sets with indexes $2i$ (for i ranging from 1 to J) denoting those sets that occupy channels. The width of channel with index $2i$ is larger than that of $2(i + 1)$ and so on. Other sets that occupy nonchannelized zones are order designated as sets with indexes $(2i + 1)$. In turn, the relationship between order-designated channelized and nonchannelized sets is in such a way that set with index $2i$ is surrounded by set with index $(2i + 1)$. Sets indexed with even and odd numbers, respectively, represent channelized and nonchannelized regions of subbasins. This distinction in indexing sets denoting channelized and nonchannelized regions represented with even and odd numbers is shown to simulate flow propagation in channelized and nonchannelized sets subsequently. This separation is physically acceptable as the directions of flow propagation are orthogonal to each other. With this reordering of simple indexing, following equations are proposed to simulate flow fields alternatively in channelized and nonchannelized regions by incrementing the set indexes:

$$\begin{aligned}
 C_{\text{flow}} &= \bigcup_{n=0}^K \{[\partial^n(S_1)] \cap S_{2i}\}, & NC_{\text{flow}} &= \bigcup_{n=0}^N \{[\partial^n(S_{2i})] \cap S_{2i+1}\}, & \text{when } i = 1, \\
 C_{\text{flow}} &= \bigcup_{n=K+1}^P \{[\partial^n(S_1)] \cap S_{2i}\}, & NC_{\text{flow}} &= \bigcup_{n=0}^N \{[\partial^n(S_{2i})] \cap S_{2i+1}\}, & \text{when } i = 2, \\
 C_{\text{flow}} &= \bigcup_{n=P+1}^Q \{[\partial^n(S_1)] \cap S_{2i}\}, & NC_{\text{flow}} &= \bigcup_{n=0}^N \{[\partial^n(S_{2i})] \cap S_{2i+1}\}, & \text{when } i = 3, \\
 C_{\text{flow}} &= \bigcup_{n=Q+1}^N \{[\partial^n(S_1)] \cap S_{2i}\}, & NC_{\text{flow}} &= \bigcup_{n=0}^N \{[\partial^n(S_{2i})] \cap S_{2i+1}\}, & \text{when } i = 4,
 \end{aligned} \tag{3.1}$$

where, in channelized flow, $n = 0 \leq K \leq P \leq Q \leq \dots \leq N$, and in nonchannelized flow $0 \leq n \leq N$. The positive integers N , K , P , and Q are mask- and marker-sets' size and shape dependent. Under the changing i , N is variable from one cycle to another cycle, and $0 \ll K \ll (K + n) \ll (P + n) \ll (Q + n) \ll \dots \ll N$.

By following set of equations in (3.1), the basic flow fields are simulated for synthetic basin (see Figures 1(c), 1(f)). The time sequential water-front propagation is simulated systematically according to following steps:

Step 1. Inlet point or set S_1 from which the water flows into basin.

Step 2. Mask set (S_2) that would be flooded from the water flowing from S_1 (marker set).

Step 3. Set S_3 —nonchannelized set of set S_2 —that acts as a mask set that gets flooded due to the water propagates from marker set S_2 .

Step 4. Set S_4 —the mask set that gets flooded due to the water flows from the marker set S_1 that already fills the set S_2 and S_3 completely.

Step 5. Set S_5 —nonchannelized set of set S_4 gets flooded from the marker set S_4 .

Step 6. Set S_6 that acts as mask set to allow the water flows from the extreme tips of set S_4 .

Step 7. Set S_7 the mask set of channelized set S_6 —here the mask set S_7 would be progressively flooded from the water flowing from the marker set S_6 .

Step 8. Channelized mask set S_8 in which the water flows from the extremities of set S_6 , and mask set S_9 of set S_8 —gets progressively flooded due to water flowing from set S_8 that acts as a marker set to fill the water in its corresponding mask set S_9 .

This is a recursive process—until the process reaches idempotence—in which the sets with odd- and even-numbered indexes, respectively, represent the zones occupied by channelized and nonchannelized regions. Direction-specific flow fields are obvious from Figures 6(b) and 6(c). Characterization of these direction-specific flow fields separately in time sequential mode would offer potentially innovative insights further to understand the relationships (i) between the flow fields, and (ii) between the induced forcing and spatial organization of flow fields. It is intuitively true that the evolution of flow fields, with increasing degree of forcing, and their spatiotemporal organization can be better linked with time-dependent morphological processes that occur due to time-dependent exogenic processes. In reality, however, the velocity of flow fields in channelized zones is usually more than that of nonchannelized zones. This variation in velocity is attributed to the fact that these two zones act like two different media with variations in surficial roughness characteristics, and minor topographic effects, and depths. Hence, defining the size of the structuring element synchronizing the velocity characteristics is an important task that needs to be addressed.

Central San Francisco Bay. The proposed framework has been implemented within a part of Central San Francisco Bay bathymetry to generate flow fields using geodesic (marker-mask) propagation. Permissions to use the images (see Figures 8(a) and 8(b)) have been obtained from USGS team. The bathymetric data of Central San Francisco Bay (see Figures 8(b), 8(c)) (USGS data) mapped by using the high-resolution multibeam swath mapping system is employed to test the framework proposed in this paper. A part essentially at the mouth of the bay from which the tidal flow fields enter into bay is considered (blocked region in Figure 8(b)). This part has various depth zones ranging from the depth of -115 meters to -14 meters. This bathymetric map that is available in grey-scale form, with darker zones representing more depth than brighter zones being shallower, is converted broadly into seven regrouped zones by following thresholding technique. The grey level ranges with the depth ranges include $0-33 = (-115)$ to (-106) m; $34-59 = (-105)$ to (-91) m; $60-100 = (-90)$ to (-68) m; $101-150 = (-67)$ to (-46) m; $151-201 = (-45)$ to (-27) m; $202-233 = (-26)$ to (-15) m;

and 234–255 = (−14) to (0 m). By choosing threshold values from the upper limits of these ranges, we decomposed the considered bathymetric image into threshold bathymetric zones as S_1, S_2, \dots, S_7 as we have chosen seven threshold grey values. Considering S_i as marker set, and S_{i+1} as mask set, flow fields are simulated in each of the threshold bathymetric zones according to the algorithm detailed in Sections 2 and 3 (see Figure 8(g)).

Coastal Santa Cruz region. A minor basin of which the discharges are flowing into sea and consist of elevation ranges between 1 and 263 meters is considered. This basin is further decomposed into sets by choosing certain threshold ranges (see Table 1). By following the framework implemented for previous cases, flow fields are generated for this minor basin (see Figure 8(h)). In the dilation process, we have opted octagonal structuring template to simulate flow fields in both San Francisco Bay and Santa Cruz DEM cases (see Figures 8(g) and 8(h)). Basic details, such as the types of basins, the elevation ranges with corresponding grey values, and ranges of threshold values employed to decompose the basins into sets, type of structuring element used to generate geodesic flow fields, and number of flow fields generated within each decomposed set, are given in Table 1.

4. Geodesic flow function analysis

4.1. Properties of geodesic flow fields in geophysical basin

For basins like simple Cases 1, 2, Central San Francisco Bay, and Santa Cruz region, for all $n \geq 1$ and $i \geq 1$,

$$\begin{aligned} (S_i) \subseteq [(S_i \oplus nB) \cap S_{i+1}] \subseteq [(S_i \oplus (n+1)B) \cap S_{i+1}] \subseteq \dots \subseteq [(S_i \oplus NB) \cap S_{i+1}] \subseteq [S_{i+1}] \\ \subseteq [(S_{i+1} \oplus nB) \cap S_{i+2}] \subseteq [(S_{i+1} \oplus (n+1)B) \cap S_{i+2}] \subseteq \dots \subseteq [(S_{i+1} \oplus NB) \cap S_{i+2}] \subseteq [S_{i+2}] \\ \subseteq [(S_{i+2} \oplus nB) \cap S_{i+3}] \subseteq [(S_{i+2} \oplus (n+1)B) \cap S_{i+3}] \subseteq \dots \subseteq [(S_{i+2} \oplus NB) \cap S_{i+3}] \subseteq \dots \end{aligned} \quad (4.1)$$

For Case 3, when $i = 1$, and $0 \leq K \leq P \leq Q \leq N$:

$$\begin{aligned} C_{\text{flow}} = (S_1) \subseteq [(S_1 \oplus kB) \cap S_{2i}] \subseteq [(S_1 \oplus (k+1)B) \cap S_{2i}] \subseteq \dots \subseteq [(S_1 \oplus KB) \cap S_{2i}] \subseteq [S_{2i}]; \\ NC_{\text{flow}} = [(S_{2i} \oplus nB) \cap S_{2i+1}] \subseteq [(S_{2i} \oplus (n+1)B) \cap S_{2i+1}] \subseteq \dots \subseteq [(S_{2i} \oplus NB) \cap S_{2i+1}] \subseteq [S_{2i+1}]. \end{aligned} \quad (4.2)$$

When $i = 2$, and $0 \leq K \leq P \leq Q \leq N$:

$$\begin{aligned} C_{\text{flow}} = [(S_1 \oplus KB) \cap S_{2i}] \subseteq [(S_1 \oplus (K+1)B) \cap S_{2i}] \subseteq \dots \subseteq [(S_1 \oplus PB) \cap S_{2i}] \subseteq [S_{2i}]; \\ NC_{\text{flow}} = [(S_{2i} \oplus nB) \cap S_{2i+1}] \subseteq [(S_{2i} \oplus (n+1)B) \cap S_{2i+1}] \subseteq \dots \subseteq [(S_{2i} \oplus NB) \cap S_{2i+1}] \subseteq [S_{2i+1}]. \end{aligned} \quad (4.3)$$

When $i = 3$, and $0 \leq K \leq P \leq Q \leq N$:

$$\begin{aligned} C_{\text{flow}} = [(S_1 \oplus PB) \cap S_{2i}] \subseteq [(S_1 \oplus (P+1)B) \cap S_{2i}] \subseteq \dots \subseteq [(S_1 \oplus QB) \cap S_{2i}] \subseteq [S_{2i}]; \\ NC_{\text{flow}} = [(S_{2i} \oplus nB) \cap S_{2i+1}] \subseteq [(S_{2i} \oplus (n+1)B) \cap S_{2i+1}] \subseteq \dots \subseteq [(S_{2i} \oplus NB) \cap S_{2i+1}] \subseteq [S_{2i+1}]. \end{aligned} \quad (4.4)$$

When $i = 4$, and $0 \leq K \leq P \leq Q \leq N$:

$$\begin{aligned} C_{\text{flow}} = [(S_1 \oplus QB) \cap S_{2i}] \subseteq [(S_1 \oplus (Q+1)B) \cap S_{2i}] \subseteq \dots \subseteq [(S_1 \oplus NB) \cap S_{2i}] \subseteq [S_{2i}]; \\ NC_{\text{flow}} = [(S_{2i} \oplus nB) \cap S_{2i+1}] \subseteq [(S_{2i} \oplus (n+1)B) \cap S_{2i+1}] \subseteq \dots \subseteq [(S_{2i} \oplus NB) \cap S_{2i+1}] \subseteq [S_{2i+1}]. \end{aligned} \quad (4.5)$$

Table 1: Details of synthetic and realistic digital topographies considered with their grey levels' and corresponding elevation/or depth ranges, and entropy values estimated for each threshold elevation/depth decomposed set of each digital topographic basin.

Case	Type	Dyn range	No. dec	Grey value range	Elevation range (m)	Used SE	No. flow field	Entropy
Case 1	Synthetic	0-1	1	0-1	0-1	Rhombus	113	2.014109
Case 2	Synthetic	0-3	3	0-1	0-1	Rhombus	97	0.335195
				1-2	2		39	0.666177
				2-3	3		46	0.987891
Case 3	Synthetic	0-7	8	0-1	0-1	Rhombus	108	0.174197
				1-2	2		39	0.421361
				2-3	3		67	0.136298
				3-4	4		32	0.272975
				4-5	5		90	0.164091
				5-6	6		29	0.562372
				6-7	7		14	0.122462
				7-8	8		17	0.332124
SF-Bay	Bathymetry	0-255	7	0-33	-115 to -106	Octagon	34	0.048562
				34-59	-105 to -91		146	0.593921
				60-100	-90 to -68		57	0.365169
				101-150	-67 to -46		57	0.604285
				151-201	-45 to -27		23	0.304051
				202-233	-26 to -15		56	0.321996
				234-255	-14 to 0		22	0.120496
SC-Topo	Topography	0-255	14	0-1	0-1	Octagon	60	0.084891
				2-14	2-14		65	0.150806
				15-34	15-35		36	0.163969
				35-65	36-67		36	0.147204
				66-85	68-88		32	0.131617
				86-102	89-105		31	0.11603
				103-124	106-128		35	0.190187
				125-157	129-162		73	0.239391
				158-182	163-188		27	0.288595
				183-197	189-203		12	0.130263
				198-212	204-218		17	0.129661
213-239	219-246	18	0.104142					
240-252	247-260	11	0.078623					
253-255	261-263	7	0.024073					

4.2. Geodesic flow spectrum

Area of each TER ($A[S_i]$) is estimated according to $\sum_{x,y} S_i(x,y)$, and area of all the TERs ($A[\sum_{i=1}^J S_i]$) is estimated as $\sum_{i=1}^J \sum_{x,y} S_i(x,y)$. For simplicity, we write these areas, respectively, as

$A[S_i]$ and $A[\sum_{i=1}^J S_i]$. $A[(S_i \oplus nB) \cap S_{i+1}]$ increases as n (cumulative effect of flood forcing after n th-time step) increases, where $A(\cdot)$ denotes finite set of cardinality. These areas are normalized by the area $A[\sum_{i=1}^J S_i]$ of basin (f). For a flat basin with no distinction in the mean elevations of channelized and nonchannelized regions (e.g., see Figures 1(a), 1(d)), the cumulative area flooded after n th time is estimated as $A[(S_i \oplus nB) \cap S_{i+1}]$, where nB is a symmetric structuring element with certain characteristic information, and S_i, S_{i+1} , respectively, denote marker set and mask set (e.g., see Figures 3 and 4(a)). Whereas, when the elevation distinction between the channelized and nonchannelized regions (e.g., see Figures 1(c), 1(f)) is realized, the cumulative area flooded in channelized region after n th time (iteration) is estimated as $A[(S_1 \oplus nB) \cap S_{2i}]$. Similarly, in the nonchannelized region, the area is estimated as $A[(S_{2i} \oplus nB) \cap S_{2i+1}]$, where $i = 1, 2, \dots, N$, and the marker sets for flow field propagation simulations are the sets indexed with $2i$, and these sets are geodesically dilated with reference to the mask sets indexed with $(2i + 1)$. The area of f is estimated as $A(f) = \sum_{(x,y)} f(x, y)$. These calculations for all the cases are plotted as functions of time (see Figure 9(f)).

Geodesic flow spectrum is the area embedded between the successive flow fields. This spectrum of decomposed elevation set (S_i) with structuring element B of radius n denoted as $GS_{S_i(n,B)}$, and is defined as follows: $GS_{S_i(n,B)} = A[(S_i \oplus (n+1)B) \cap (S_{i+1})] - A[(S_i \oplus (n)B) \cap (S_{i+1})]$. Then, the probability is derived as follows: $P_{S_i(B)} = GS_{S_i(n,B)} / A[\sum_{i=1}^J S_i]$, where $i = 1, 2, 3, \dots, J$. The decomposed set-wise entropy with respect to total area of all the sets—decomposed from the function—is defined as $H/(S_i, B) = -\sum_{n=0}^N P_{S_i(n,B)} \log P_{S_i(n,B)}$. Entropy values estimated by considering the probabilities that are computed with respect to the whole basin are given in the last column of Table 1. From this spectrum, a one-dimensional path support of different TERs and adjacent TERs—morphological structures of the basins can be better understood. A potentially valuable insights and links with instantaneous unit hydrography can be explored. These functions provide general geodesic distribution pattern between the TERs. It is conspicuous that each geodesic function exhibits distinct pattern, which further explains that geodesic function of each TER is someway similar to geomorphic width function.

5. Results and discussion

Areas embedded between the successive flow fields are divided by the total area of corresponding threshold bathymetry zone to estimate the probability distribution values and further the entropy values. In turn, the probability distribution values of each threshold bathymetry region (TBR) are plotted as functions of discrete time steps to understand the rates of change in the areas between the flow fields of corresponding TBR (see Figures 9(a)–9(e)). From these plots, it is obvious that the larger is the peak, the wider is the area embedded between the successive flow fields. It is also observed that these probability distribution values, and hence entropy values are marker-mask sets' dependent. The geometric relationship between the marker and mask sets as well as the structuring element's characteristic information influences the general flow fields' spatial organization, which further affects the probabilities and entropy values. The rate of change in the areas embedded between the flow fields, simulated from a single marker set, is estimated in terms of probability distribution values. It is hypothesized that the zones with abrupt changes in the probability patterns attribute to the fact that these zones support occurrence of unusual suspended sediment patterns, due to high degree of spatial complexity of the flow fields. These zones as demarcated in the graph(s) further facilitate proper categorization of either surficial or bottom topographic zones—in terms of zones that are prone to have varied

degrees of sensitivities to perturbation from dominating inflows such as tidal flow, river flow, and flow due to flooding and so forth.

Total area flooded after each cycle of geodesic propagation is estimated and plotted as function of discrete time for all the five considered cases (see Figure 9(f)). It is obvious that the rates of change in the flow fields' pattern in the considered cases are different. Such variations are attributed to the spatial and topographic complexities of basins. This analysis facilitates new insights to explore links between general statistical measures (e.g., probabilities and entropy values), and dynamics of sediment inflow patterns within each TBR and the morphological constitution of tidal and floodplain basins across times, since surficial process involved therein is highly time dependent. In summary, we provide a framework, which can be tested on any basin by using very high-resolution DEM/DBM data at different time periods (perhaps during pre-flood or post-flood times and low-tide or high-tide time periods) that generally reflect the surficial morphology of the floodplain or tidal basin as the process involved there is time-dependent in contrast to that of basins in fluvial environment.

In cases where topography or bathymetry of basins is not available, and instead remote sensing data is used, a simplified method of estimation of the flow fields within the basin, neglecting the bathymetry, becomes helpful [25]. However, the flow fields simulated by merely considering basin as flat surface would be directly determined by the boundary of the basin alone. If one cross checks the flow fields simulated with an assumption that the bottom topography is completely flat with that of the flow fields estimated from the topographic/bathymetric data, one realizes how the former is entirely dependent on the boundary of the basin. In fact, the two flow fields are highly contrasting as shown in Figures 8(f) and 8(g). If topographic data of basin (or inlets, estuaries, and bays) are available at multitemporal mode, the flow field can be simulated via geodesic method as proposed here to study the spatiotemporal dynamics of the topography. Very high-resolution DEM (e.g., retrieved from Shuttle Radar Topography Mission (SRTM)) provides subtle changes in topographic elevation. Usually the elevation differences within floodplain environment and in tidal environment are minor. However, the morphological variations within such environments are highly time dependent. This time-dependent variations may synchronize the fluctuating hydrological flows that are usually influenced due to flooding/tide patterns of the system. We provide a basic framework to simulate flow fields via geodesic morphological concepts, which require prior processing of basin to decompose it into thresholded sets and indexing them accordingly. This prior processing could be done by simple image threshold decomposition procedures. Furthermore, this framework has been applied to generate flow fields on three simulated basins and on two digital topographies of San Francisco Bay and Santa Cruz region. Space-time structures of flow fields in basins that occur due to changes in inflow patterns can be treated as a coupled-dynamical system.

6. Conclusions

We proposed a framework, based on geodesic morphologic transformations, to characterize discrete geophysical basins of surficial and bathymetric types. The three phases of the framework include (i) decomposition of digital topographic basin into sets through thresholding technique, (ii) generation of geodesic flow fields within each set successively, and (iii) estimation of probabilities of areas being embedded between flow fields of each set and the successive sets. We tested this three-phase framework on several synthetic and realistic digital

topographic basins. Results derived include construction of geodesic basin functions that can be treated as a new basin descriptor, which can be further linked with geomorphic width function. These geodesic functions depend on the (i) general structure of basin function, (ii) the geometric organization, and their internal spatial relationships of TERs, and (iii) structure of geodesic propagation (frontlines). These functions can be employed to obtain new insights into modeling the sediment transport and deposition processes, morphologic processes that control the morphologic development of basin function. This approach can be adopted in studies related to understanding of morphodynamical processes in a quantitative fashion when topographies of basins are available at higher spatial resolutions. This approach complements with other existing geomorphometric techniques that provide quantitative treatment of the morphology of basin-wise topographies. To provide main interpretation of these geodesic functions of basin-wise topographies and relationships with other mathematical properties which are widely studied in the context of studying the basin structure will be an open problem.

Appendix

In this appendix, we provide illustrations (see Figures 10 and 11) of basic details on (1) threshold decomposition of digital topography and isolation of threshold sets, and (2) morphological transformations in matrix forms. These illustrations are given for better understanding of equations (2.1)–(2.4) and results shown in Figures 3–7. We also provide the list of symbols and notations at the end of this Appendix.

Figure 10 depicts original image f which has maximum intensity level $J = 4$. Threshold decomposed zones f_j with $j = 1, 2, 3, 4$, and 5 ($J + 1$) are, respectively, shown along with the isolated sets with index i ranging from $1, 2, \dots, J$. The sets S_i are isolated by $f_j - f_{j+1}$.

Figure 11 depicts matrix representation of morphological dilation and involved translates. Figure 11(a) illustrates this transformation with possible translates of s_i by b , the union of which yields an expanded version of S_i . In this transformation $-B = \{-b : b \in B\}$, that is, B is rotated 180° about the origin. Here, while matching the first encountered set element at location $(1, 2)$ with reference to centre point of B , we check for exact overlap with all points in B with all points. As for the first encountered set element, we see that there is a mismatch. Then, the points of B that are not exactly matched with elements would be placed at locations beyond the set elements. This can be better comprehended from the first translate shown in Figure 11(a). Similarly, the second and further translates are shown. As at the third encountered element, the matching is exactly identified by means of B , there is no change observed in the corresponding translate. The union of all these translates produces dilated version of S_i by B as illustrated in matrix form (see Figure 11(b)). Instead of using a larger B to simulate propagation of flow with greater velocity, with the use of smaller B repeatedly, one will get the same effect. The cumulative B , of which the diagrammatic representation is shown in Figure 11(b), is mathematically represented in (4). Iterative dilations for n times are represented as $(S_i \oplus nB)$. The role of B that functions as an interface between S_i and isotropic propagation is to simulate the effects of flow field propagation.

List of symbols and notations

$|R^d$: Euclidean space

f : Function of basin represented as digital topographic image

- s, x, b : Points of $|R^d$
 S, X, B : Subsets of $|R^d$
 j : Index—representing threshold value— $j = 0, 1, 2, \dots, J$
 i : Index—representing isolated threshold set— $i = 0, 1, 2, \dots, J$
 J : Maximum nonnegative intensity (elevation) value
 S^c : Complement of S in $|R^d$
 S_s : S shifts by $\vec{o}s$ (o = origin of $|R^d$)
 \cup, \cap, \setminus : Logical union, logical intersection, and logical difference
 \subseteq : Improper subset
 \subset : Subset
 $S \cup X$: Union of S and X
 $S \cap X$: Intersection of S and X
 $S \setminus X$: Set difference of S and X
 nB : n th-size structuring element symmetric w.r.t origin at center
 $1B$: Primitive element with origin at center, and radius 1
 NB : Largest size of structuring element
 \oplus : Dilation
 $S \oplus B = \bigcup_{b \in B} S_b$: Morphological dilation of S w.r.t. B
 ∂S : Boundary of S
 C_{flow} : Channel flow
 NC_{flow} : Nonchannel flow
 TB_{flow} : Flow in the tidal basin
 \emptyset : Empty set
 n : Iteration/cycle number (or radius of structuring element, where $n = 0, 1, 2, \dots, N$)
 N : Maximum iteration/cycle number required for transforming a set into the state of idempotence
 $A(\cdot)$: Finite set of cardinality

Acknowledgments

The authors gratefully acknowledge the comments and suggestions provided by Jean Serra, Arthur Cracknell, Prasad Patnaik, and four anonymous reviewers which have strengthened the manuscript. Authors are also grateful to Volkan Sevilgen and Pete Dartnell of United States Geological Survey for granting permission to use Central San Francisco Bay DBM data and Santa Cruz DEM data.

References

- [1] L. C. Graham, "Synthetic interferometer radar for topographic mapping," *Proceedings of the IEEE*, vol. 62, no. 6, pp. 763–768, 1974.
- [2] H. A. Zebker and R. M. Goldstein, "Topographic mapping from interferometric synthetic aperture radar observations," *Journal of Geophysical Research*, vol. 91, no. B5, pp. 4993–4999, 1986.
- [3] A. P. Cracknell, "Remote sensing techniques in estuaries and coastal zones—an update," *International Journal of Remote Sensing*, vol. 20, no. 3, pp. 485–496, 1999.
- [4] N. K. Tripathi and A. M. Rao, "Bathymetric mapping in Kakinada Bay, India, using IRS-1D LISS-III data," *International Journal of Remote Sensing*, vol. 23, no. 6, pp. 1013–1025, 2002.
- [5] S. Bagheri, M. Stein, and R. Dios, "Utility of hyperspectral data for bathymetric mapping in a turbid estuary," *International Journal of Remote Sensing*, vol. 19, no. 6, pp. 1179–1188, 1998.

- [6] A. C. B. Roberts, "Shallow water bathymetry using integrated airborne multi-spectral remote sensing," *International Journal of Remote Sensing*, vol. 20, no. 3, pp. 497–510, 1999.
- [7] C. J. Calkoen, G. H. F. M. Hesselmanns, G. J. Wensink, and J. Vogelzang, "The bathymetry assessment system: efficient depth mapping in shallow seas using radar images," *International Journal of Remote Sensing*, vol. 22, no. 15, pp. 2973–2998, 2001.
- [8] B. Thibault, P. Larouche, and J.-M. M. Dubois, "Variability of hydrodynamic phenomena of the Upper St. Lawrence estuary using Landsat 5 Thematic Mapper data," *International Journal of Remote Sensing*, vol. 23, no. 3, pp. 511–524, 2002.
- [9] C. R. Duguay and P. M. Lafleur, "Determining depth and ice thickness of shallow sub-Arctic lakes using space-borne optical and SAR data," *International Journal of Remote Sensing*, vol. 24, no. 3, pp. 475–489, 2003.
- [10] G. Ferrier, J. T. Macklin, S. P. Neill, A. M. Folkard, G. J. M. Copeland, and J. M. Anderson, "Cover: observing estuarine currents and fronts in the Tay Estuary, Scotland, using an airborne SAR with along-track interferometry (ATI)," *International Journal of Remote Sensing*, vol. 26, no. 20, pp. 4399–4404, 2005.
- [11] W. H. F. Smith and D. T. Sandwell, "Bathymetric prediction from dense satellite altimetry and sparse shipboard bathymetry," *Journal of Geophysical Research*, vol. 99, no. B11, pp. 803–824, 1994.
- [12] L. E. Band, "Topographic partition of watersheds with digital elevation models," *Water Resources Research*, vol. 22, no. 1, pp. 15–24, 1986.
- [13] L. Vincent and P. Soille, "Watersheds in digital spaces: an efficient algorithm based on immersion simulations," *IEEE Transactions on Pattern Analysis and Machine Intelligence*, vol. 13, no. 6, pp. 583–598, 1991.
- [14] L. Fatale, J. R. Ackeret, and J. Messmore, "Impact of digital terrain elevation data (DTED) resolution on army applications: simulation vs. reality," in *Proceedings of the American Congress on Surveying and Mapping (ACSM '94)*, pp. 89–104, Reno, Nev, USA, April 1994.
- [15] R. Stone and J. Dugundji, "A study of microrelief—its mapping, classification, and quantification by means of a Fourier analysis," *Engineering Geology*, vol. 1, no. 2, pp. 89–187, 1965.
- [16] D. L. Turcotte, *Fractals and Chaos in Geology and Geophysics*, Cambridge University Press, Cambridge, UK, 2nd edition, 1997.
- [17] L. T. Tay, B. S. D. Sagar, and H. T. Chuah, "Derivation of terrain roughness indicators via granulometries," *International Journal of Remote Sensing*, vol. 26, no. 18, pp. 3901–3910, 2005.
- [18] L. T. Tay, B. S. D. Sagar, and H. T. Chuah, "Granulometric analyses of basin-wise DEMs: a comparative study," *International Journal of Remote Sensing*, vol. 28, no. 15, pp. 3363–3378, 2007.
- [19] J. H. Perera, *The hydrogeomorphic modeling of sub surface saturation excess runoff generation*, Ph.D. thesis, University of Newcastle, Newcastle, Australia, 1997.
- [20] M. Marani, A. Rinaldo, R. Rigon, and I. Rodriguez-Iturbe, "Geomorphological width functions and the random cascade," *Geophysical Research Letters*, vol. 21, no. 19, pp. 2123–2126, 1994.
- [21] I. Rodriguez-Iturbe and A. Rinaldo, *Fractal River Basins: Chance and Self-Organization*, Cambridge University Press, Cambridge, UK, 1997.
- [22] D. Veneziano, G. E. Moglen, P. Furcolo, and V. Iacobellis, "Stochastic model of the width function," *Water Resources Research*, vol. 36, no. 4, pp. 1143–1157, 2000.
- [23] L. Chockalingam and B. S. D. Sagar, "Morphometry of network and nonnetwork space of basins," *Journal of Geophysical Research*, vol. 110, no. B8, Article ID B08203, 15 pages, 2005.
- [24] L. T. Tay, B. S. D. Sagar, and M. T. Chuah, "Allometric relationships between traveltime channel networks, convex hulls, and convexity measures," *Water Resources Research*, vol. 42, no. 6, Article ID W06502, 8 pages, 2006.
- [25] S. Fagherazzi, P. L. Wiberg, and A. L. Howard, "Tidal flow field in a small basin," *Journal of Geophysical Research*, vol. 108, no. C3, Article ID 3071, 10 pages, 2003.
- [26] P. Blondeaux and G. Vittori, "Flow and sediment transport induced by tide propagation—1: the flat bottom case," *Journal of Geophysical Research*, vol. 110, no. C7, Article ID C07020, 13 pages, 2005.
- [27] P. Blondeaux and G. Vittori, "Flow and sediment transport induced by tide propagation—2: the wavy bottom case," *Journal of Geophysical Research*, vol. 110, no. C8, Article ID C08003, 11 pages, 2005.
- [28] http://sfbay.wr.usgs.gov/highlight_archives/new1998.html.
- [29] <http://terraweb.wr.usgs.gov/projects/SFBaySonar>.
- [30] <http://bard.wr.usgs.gov/html/dir/dem.html/index.html>.
- [31] <http://rockyweb.cr.usgs.gov/nmpstds/acrodcs/dem/1DEM0897.PDF>.

- [32] P. A. Maragos and R. D. Ziff, "Threshold superposition in morphological image analysis systems," *IEEE Transactions on Pattern Analysis and Machine Intelligence*, vol. 12, no. 5, pp. 498–504, 1990.
- [33] C. Lantuejoul and F. Maisonneuve, "Geodesic methods in quantitative image analysis," *Pattern Recognition*, vol. 17, no. 2, pp. 177–187, 1984.
- [34] J. A. Sethian, *Level Set Methods and Fast Marching Methods*, vol. 3 of *Cambridge Monographs on Applied and Computational Mathematics*, Cambridge University Press, Cambridge, UK, 2nd edition, 1999.
- [35] J. Serra, *Image Analysis and Mathematical Morphology*, Academic Press, London, UK, 1982.

Special Issue on Modeling Experimental Nonlinear Dynamics and Chaotic Scenarios

Call for Papers

Thinking about nonlinearity in engineering areas, up to the 70s, was focused on intentionally built nonlinear parts in order to improve the operational characteristics of a device or system. Keying, saturation, hysteretic phenomena, and dead zones were added to existing devices increasing their behavior diversity and precision. In this context, an intrinsic nonlinearity was treated just as a linear approximation, around equilibrium points.

Inspired on the rediscovering of the richness of nonlinear and chaotic phenomena, engineers started using analytical tools from "Qualitative Theory of Differential Equations," allowing more precise analysis and synthesis, in order to produce new vital products and services. Bifurcation theory, dynamical systems and chaos started to be part of the mandatory set of tools for design engineers.

This proposed special edition of the *Mathematical Problems in Engineering* aims to provide a picture of the importance of the bifurcation theory, relating it with nonlinear and chaotic dynamics for natural and engineered systems. Ideas of how this dynamics can be captured through precisely tailored real and numerical experiments and understanding by the combination of specific tools that associate dynamical system theory and geometric tools in a very clever, sophisticated, and at the same time simple and unique analytical environment are the subject of this issue, allowing new methods to design high-precision devices and equipment.

Authors should follow the Mathematical Problems in Engineering manuscript format described at <http://www.hindawi.com/journals/mpe/>. Prospective authors should submit an electronic copy of their complete manuscript through the journal Manuscript Tracking System at <http://mts.hindawi.com/> according to the following timetable:

Manuscript Due	December 1, 2008
First Round of Reviews	March 1, 2009
Publication Date	June 1, 2009

Guest Editors

José Roberto Castilho Piqueira, Telecommunication and Control Engineering Department, Polytechnic School, The University of São Paulo, 05508-970 São Paulo, Brazil; piqueira@lac.usp.br

Elbert E. Neher Macau, Laboratório Associado de Matemática Aplicada e Computação (LAC), Instituto Nacional de Pesquisas Espaciais (INPE), São José dos Campos, 12227-010 São Paulo, Brazil ; elbert@lac.inpe.br

Celso Grebogi, Center for Applied Dynamics Research, King's College, University of Aberdeen, Aberdeen AB24 3UE, UK; grebogi@abdn.ac.uk